



Large Eddy Simulation of Molten Steel Flow and Inclusion Transport in a New Butterfly-Type Induction Heating Tundish

NING WANG, ZHONGQIU LIU, HUANG CHENG, FENGSHENG QI, CHANGJUN WANG, LI ZHANG, and BAOKUAN LI

In addressing the retrofitting issues of conventional non-induction heating tundish, a novel butterfly-type induction heating tundish model was devised. A three-dimensional coupled mathematical model of magnetic, thermal, and fluid fields was established to investigate the temperature distribution, flow characteristics, and temperature rise curves within the butterfly-type tundish. The model for inclusion motion and removal, based on Large Eddy Simulation (LES), was devised, integrating factors such as normal critical velocity, coefficient of restitution, and critical incident angle at the wall boundary conditions to provide a more precise depiction of the reflection and adsorption processes of inclusions on the tundish wall. The findings suggest that induction heating can effectively offset the temperature loss of the molten steel and enhance the removal rate of inclusions, particularly those of large size. The outlet temperature increases by -15 K, 7 K, 15 K, and 26 K, and the total removal rate of inclusions reaches 69.18, 83.37, 87.69, and 92.01 pct at 0, 600, 800, and 1000 kW, respectively. The channel serves as the primary site for inclusion removal when employing induction heating. Among these, the removal rates within the channel and at the slag layer exhibit a positive correlation with the inclusion diameter, while the remaining wall removal rates show a negative correlation. The implementation of induction heating technology leads to a notable decrease in the entry of large-sized inclusions into the mold.

<https://doi.org/10.1007/s11663-024-03201-3>

© The Minerals, Metals & Materials Society and ASM International 2024

I. INTRODUCTION

THE tundish has been extensively utilized as a secondary refining vessel, tasked with optimizing the flow field, compensating for temperature loss, removing inclusions, and performing other functions.^[1–3] In traditional tundish without induction heating devices, weirs, dams, baffles, and turbulence suppressors have been widely utilized to optimize the flow field, prolong the residence time of molten steel, and facilitate the removal of inclusions through flotation.^[4–6] However, inevitably, as the molten steel flows, it undergoes heat exchange with the environment, resulting in considerable heat loss that prevents the molten steel from reaching the required overheating temperature before

entering the mold. Therefore, it is crucial to compensate for the heat loss of the molten steel. The predominant heating methods mainly comprise plasma heating^[7,8] and electromagnetic induction heating. Due to its advantages of cleanliness, safety, and precise temperature control, electromagnetic induction heating has emerged as the preferred method for tundish heating.

Given the complex and unpredictable nature of fluid dynamics and heat transfer phenomena within the tundish channel during induction heating, numerical simulations have emerged as the preferred approach for research. Wang^[9] established a three-dimensional coupled mathematical model integrating magnetic, thermal, and flow to calculate the multi-physical fields in channel-type induction heating tundish. They validated key parameters like flow field and magnetic flux density field using instruments and water model experiments, obtaining temperature rise curves, temperature fields, and flow states within the tundish under various induction heating powers. Yue^[10] employed numerical simulations to investigate the temperature field, flow field, and heating characteristics of multi-strand induction heating tundish. They considered the influence of natural convection and validated the accuracy of the

NING WANG, ZHONGQIU LIU, FENGSHENG QI, CHANGJUN WANG, and BAOKUAN LI are with the School of Metallurgy, Northeastern University, Shenyang 110819, P.R. China. Contact e-mails: liuzq@smm.neu.edu.cn; libk@smm.neu.edu.cn HUANG CHENG and LI ZHANG are with the Shanghai Dongshen Metallurgy & Technology Company Limited, Shanghai 200435, P.R. China.

Manuscript submitted May 9, 2024; accepted June 25, 2024.

Article published online July 8, 2024.

computational results through industrial experiments. Chen^[11] designed a four-channel induction heating tundish based on the traditional dual-channel design. They calculated the flow field and heat transfer characteristics under various induction current intensities. The results indicated that the stability and consistency of outlet temperature rise in the four-channel tundish were superior to those in the dual-channel design. Zhang^[12] employed numerical simulations to conduct an in-depth investigation into the squeezing effect in channel-type induction heating tundish. The results indicated that the eccentric electromagnetic force resulted in the formation of single/double recirculation zones within the channel, leading to a significant stirring effect on the molten steel.

Inclusions significantly influence the properties of steel products, resulting in issues such as reduced ductility and stress concentration. To guarantee the quality of cast billets, it is imperative to rigorously control the quantity of inclusions within a specific range, especially large-sized inclusions. While baffles can enhance the flow morphology of molten steel and improve the removal rate of inclusions, the flushing of molten steel against the baffles may introduce additional inclusions. Hence, research on the motion and removal of inclusions within the tundish, particularly in induction heating tundish, is crucial.^[13] However, due to the variability and complexity of particle multiphase system motion morphology, traditional experimental methods make it challenging to deeply investigate their internal motion mechanisms, resulting in many processes running as “black boxes” numerical simulations are currently an effective and relatively accurate method. Wang^[14] investigated the motion and removal process of inclusions with various diameters within the channel-type induction heating tundish. They observed that the removal of inclusions primarily takes place within the channel, with a more pronounced removal effect for large-sized inclusions. Collision growth, thermophoretic force, and electromagnetic force all exert significant influences on the removal rate of inclusions within the channel. Zhang^[15] divided the tundish into two regions with different removal mechanisms to calculate the removal of inclusions. They considered three removal methods: flotation to the free surface, agglomeration and growth, and lining adhesion. Finally, they validated the mathematical model using industrial experimental data. Lei^[16] utilized a mass/population conservation model of inclusions to study the physical field of inclusions. The results indicate that electromagnetic force and joule heating play a significant role in the removal rate of inclusions, with electromagnetic force having a more pronounced effect compared to joule heating. The removal rate of inclusions within the channel accounts for one third of the total removal rate. Xing^[17] designed an induction heating tundish with arc-shaped channels based on the channel-type induction heating tundish. Through numerical simulations, it was found that the induction heating tundish with arc-shaped channels exhibits significantly improved heating characteristics, residence time, and inclusion removal rate.

Currently, traditional non-induction heating tundishes are still widely used. Due to the proximity of the pouring chamber and the ladle spout, there is no space to install induction heating equipment. Therefore, it is impossible to compensate for the temperature drop of the molten steel. To address the retrofitting issues of traditional tundish, this study proposes a novel butterfly-type induction heating tundish. By adding a new intermediate chamber behind the ladle shroud, the design aims to extend the channel length, providing sufficient space to install induction heating equipment. A three-dimensional coupled mathematical model of magnetic, thermal, and fluid fields was established to investigate the temperature distribution, flow characteristics, and temperature rise curves within the butterfly-type tundish. To provide a more precise description of the flow and heat transfer phenomena within the butterfly-type tundish, this study employed the Large Eddy Simulation (LES) method to simulate the flow of molten steel. Additionally, an inclusion motion model based on LES was developed. The study considered two inclusion removal mechanisms: adsorption in the slag layer of the pouring chamber and adsorption on the wall surfaces (including the channel and other regions). Mathematical models were developed to describe the collision, reflection, and adsorption of inclusions at the wall boundaries. Additionally, various complex factors affecting inclusion removal, such as critical velocity in the normal direction, coefficient of restitution, and incident angle, were taken into account. User-defined functions (UDF) were employed to update boundary conditions. The removal rates of inclusions with various diameters at different induction heating powers and positions were determined.

II. NUMERICAL MODEL

A. Physical Model of Butterfly-Type Induction Heating Tundish

Figure 1 shows the physical model of a butterfly-type induction heating tundish. The butterfly-type induction heating tundish consists of an injection chamber, a pouring chamber, an intermediate chamber, channel No. 1, two channels No. 2, and two induction heating devices. The induction heating device comprises a detachable iron core and multi-turn coils. As shown in Figure 2, the molten steel initially enters the injection chamber *via* the inlet, proceeds into the intermediate chamber appended to the rear side of the ladle through channel No. 1, and subsequently flows into the pouring chamber through two channels No. 2 (referred to as channels hereafter). Finally, it flows into the mold through three identical immersion nozzles, completing the entire pouring process. The trajectory of molten steel throughout the entire flow process resembles that of a butterfly, hence, the term “butterfly-type” induction heating tundish. The dimensional parameters of the butterfly-type tundish are presented in Table I.

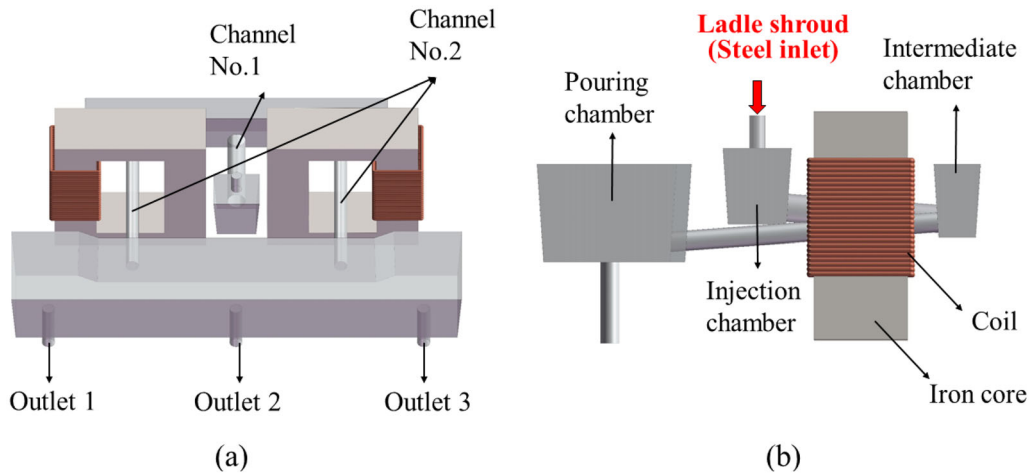


Fig. 1—Physical model of butterfly-type induction heating tundish.

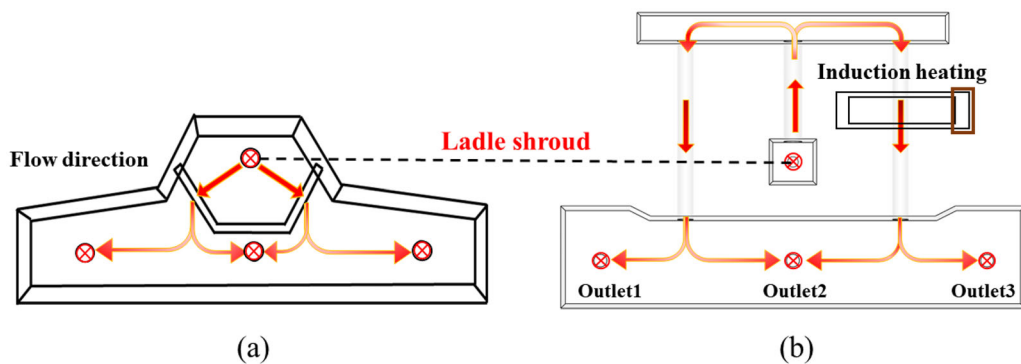


Fig. 2—The path shape of molten steel: (a) Traditional tundish (b) New butterfly-type induction heating tundish.

B. Mathematical Model

To streamline calculations and mitigate unnecessary consumption of computing resources, the following assumptions are made:

- (1) The electromagnetic materials are assumed to be isotropic, with constant physical parameters. The molten steel is considered an incompressible Newtonian fluid, with variations in steel density accounted for only by temperature changes, all other physical parameters are assumed constant.
- (2) Neglecting the fluctuations on the surface of the molten steel inside the tundish, and disregarding the effects of surface covering agents and slag layers on the flow of the molten steel.
- (3) Due to the magnetic Reynolds number being much smaller than 1, the influence of steel flow on the electromagnetic field is ignored.
- (4) The inclusion is a rigid sphere, the material is aluminum oxide, and the physical properties are constant. According to Hertz's theory, the shape and size of the contact area are related to elastic

Table I. The Size of the Butterfly-Type Tundish

Parameter	Value
Inlet Diameter/(mm)	90
Outlet Diameter/(mm)	120
Channel No. 1 Diameter/(mm)	170
Channel No. 2 Diameter/(mm)	150
maximum Length/(mm)	2950
Maximum Width/(mm)	4320
maximum Height/(mm)	1300
Channel Inclination Angle/(°)	4

deformation, so it is assumed that only elastic deformation occurs, and no plastic deformation occurs.

The Maxwell equations are the theoretical basis for electromagnetic field analysis. The steps for solving Maxwell equations and calculating induced current, joule heat, and electromagnetic force are already quite mature, and they will not be elaborated here.^[18]

1. LES model

The LES method is used to calculate the flow of molten steel in this study. The basic principle of LES is to separate and solve large-scale and small-scale vortices and filter the time-dependent N-S equation to obtain the control equation. Compared to the RANS method, LES allows for the presence of small and medium-sized transient flow structures, which can improve the accuracy of the flow field and subsequent inclusion removal calculations.^[19–22]

The continuity equation is

$$\frac{\partial \rho}{\partial t} + \nabla \cdot (\rho \mathbf{u}) = 0, \quad [1]$$

where ρ is the density of molten steel, and \mathbf{u} is the velocity of molten steel.

The momentum equation is

$$\frac{\partial(\rho \mathbf{u})}{\partial t} + \nabla \cdot (\rho \mathbf{u} \mathbf{u}) = -\nabla P + \nabla \cdot [\mu_{eff}(\nabla \mathbf{u} + \nabla \mathbf{u}^T)] - \nabla \tau_{ij} + \rho \mathbf{g}, \quad [2]$$

where μ_{eff} is the effective viscosity, which includes turbulent viscosity and molten steel viscosity. τ_{ij} is the Subgrid Stress, and \mathbf{g} is the gravity.

The LES is a spatial averaging of turbulence, which separates large-scale vortices from small-scale vortices through filtering functions. Large-scale vortices are directly simulated, while small-scale vortices are closed using mathematical models. The velocity is divided into two parts, and written in component form as follows:

$$u = \bar{u}_i + u'_i, \quad [3]$$

where \bar{u}_i is the velocity of large-scale flow, u'_i is the velocity of small-scale flow, small-scale flow needs to be described through models, while large-scale flows are controlled by filtering functions:

$$\bar{u}_i(x) = \int_D f(x; x') u_i(x') dx', \quad [4]$$

where D is the flow area, x is the spatial position vector. $f(x; x')$ is the filter function, when it is smaller than the grid scale, $f(x; x') = 1/V$, otherwise, it is 0. The filtered Navier Stokes equation is

$$\frac{\partial(\rho \bar{u}_i)}{\partial t} + \frac{\partial}{\partial x_j} (\rho \bar{u}_i \bar{u}_j) = \frac{\partial}{\partial x_j} \left(\mu \left(\frac{\partial \bar{u}_i}{\partial x_j} + \frac{\partial \bar{u}_j}{\partial x_i} \right) \right) - \frac{\partial \bar{P}}{\partial x_i} - \frac{\partial \tau_{ij}}{\partial x_j} + \rho g_i + \frac{6}{\pi d_p^3} \cdot F_i. \quad [5]$$

The subgrid scale shear stress is written in the following form:

$$\tau_{ij} = \rho \bar{u}_i \bar{u}_j - \rho \bar{u}_i \bar{u}_j. \quad [6]$$

The above equation can establish its relationship with the large-scale deformation rate tensor based on the Boussinesq hypothesis:

$$\tau_{ij} - \frac{1}{3} \tau_{kk} \delta_{ij} = 2\mu_t \bar{S}_{ij}, \quad [7]$$

$$\bar{S}_{ij} = \frac{1}{2} \left(\frac{\partial \bar{u}_i}{\partial x_j} + \frac{\partial \bar{u}_j}{\partial x_i} \right), \quad [8]$$

where μ_t is subgrid-scale (SGS) viscosity, this article uses the WALE model to solve it. Compared to the traditional Smagorinsky model, the WALE model produces almost no eddy viscosity in laminar flow with walls, so it can reproduce the transition from laminar to turbulent flow.

$$\mu_t = \rho (C_w \Delta)^2 \frac{\left(S_{ij}^d S_{ij}^d \right)^{3/2}}{\left(S_{ij}^d S_{ij}^d \right)^{5/4} + \left(\bar{S}_{ij} \bar{S}_{ij} \right)^{5/2}}, \quad [9]$$

where S_{ij}^d is the traceless symmetric part of the square of the velocity gradient tensor, and C_w is a constant with a value of 0.5.

$$S_{ij}^d = \bar{S}_{ik} \bar{S}_{kj} + \bar{\Omega}_{ik} \bar{\Omega}_{kj} - \frac{1}{3} \delta_{ij} (\bar{S}_{mn} \bar{S}_{mn} - \bar{\Omega}_{mn} \bar{\Omega}_{mn}), \quad [10]$$

where the vorticity tensor $\bar{\Omega}_{ij}$ is given by

$$\bar{\Omega}_{ij} = \frac{1}{2} \left(\frac{\partial \bar{u}_i}{\partial x_j} - \frac{\partial \bar{u}_j}{\partial x_i} \right). \quad [11]$$

2. Discrete Phase Model (DPM)

The DPM model is used to calculate the movement and removal of inclusions, treating the inclusions as a discrete phase. The motion trajectory is predicted by integrating the force balance on them and written in a Lagrangian reference frame. As shown in Figure 3, The motion law of inclusions conforms to Newton's second law:

$$m_p \frac{d\bar{\mathbf{u}}_p}{dt} = \mathbf{F}, \quad [12]$$

$$\mathbf{F} = \mathbf{F}_g + \mathbf{F}_B + \mathbf{F}_P + \mathbf{F}_D + \mathbf{F}_L + \mathbf{F}_{VM} + \mathbf{F}_T + \mathbf{F}_{EMF}, \quad [13]$$

where m_p is the mass of inclusion, \mathbf{F}_g is gravity, \mathbf{F}_B is buoyancy force, \mathbf{F}_P is pressure gradient force, \mathbf{F}_D is drag force, \mathbf{F}_L is lift force, \mathbf{F}_{VM} is virtual mass force, \mathbf{F}_T is thermophoretic force and \mathbf{F}_{EMF} is electromagnetic force, as shown in Table II.

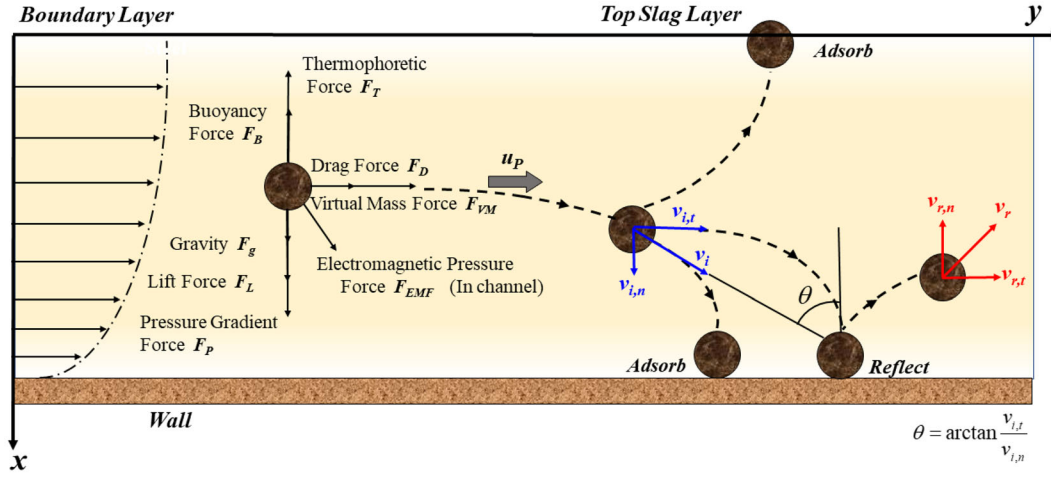


Fig. 3—Schematic diagram of stress and removal method of inclusions.

Table II. The Force Acting on Inclusion

Forces	Equations
Saffman Lift Force	$F_L = 1.61 d_p^2 (\mu_l \rho_l)^{1/2} \nabla \times \mathbf{u}_l ^{-1/2} [(\mathbf{u}_l - \mathbf{u}_p) \times (\nabla \times \mathbf{u}_l)]$
Virtual Mass Force	$F_{VM} = \frac{\pi}{6} d_p^3 \rho_l C_{VM} \left(\frac{d\mathbf{u}_l}{dt} - \frac{d\mathbf{u}_p}{dt} \right)$
Drag Force	$F_D = \frac{\pi}{8} C_D \rho_l d_p^2 \mathbf{u}_l - \mathbf{u}_p (\mathbf{u}_l - \mathbf{u}_p)$
Buoyancy Force	$F_B = \rho_l \frac{\pi}{6} d_p^3 \mathbf{g}$
Pressure Gradient Force	$F_P = \rho_p \frac{\pi}{6} d_p^3 \frac{d\mathbf{u}_l}{dt}$
Thermophoretic Force	$F_T = -6\pi \mu_l d_p \alpha \beta \nabla T$
Electromagnetic Force ^[23]	$F_{EMF} = \frac{3}{4} \frac{\pi d_p^3}{6} \mathbf{F}$

The collision between inclusions is regarded as a stochastic event, with pertinent mathematical models outlined in Li's^[24,25] research. Due to the precise capture of fluid vortices when using LES, this will be reflected in the pulsating velocity of particles. To enhance the accuracy of inclusion motion velocity and trajectory calculations, this paper adopts a random walk model grounded in LES.

The inclusion removal methods considered in this article are (1) adsorption on the tundish wall (including the channel and other regions), and (2) absorption in the top slag layer of the pouring chamber. The processes of inclusions contacting the wall, adsorption, and reflection are complex, the normal critical velocity, which determines whether reflection or adsorption occurs, is a crucial parameter. When inclusions impact the wall, if their velocity exceeds the normal critical velocity, they will expend a certain amount of kinetic energy and return to the molten steel to continue moving. If their velocity is below the normal critical velocity, they will be captured by the wall. The calculation of normal critical velocity was carried out using the Thornton and Ning model,^[26] which is related to the material of the tundish

wall and inclusion. In this study, the wall material was set as sintered magnesia ($\text{MgO} + \text{SiO}_2$), and the inclusion material was set as alumina (Al_2O_3).

$$v_{s,n} = 1.84 \left[\frac{(2\sqrt{r_1 r_2}/R)^{57}}{\rho^3 E^{*2}} \right]^{\frac{1}{6}}, \quad [14]$$

$$E^* = \frac{1}{\frac{1-v_1^2}{E_1} + \frac{1-v_2^2}{E_2}}, \quad [15]$$

where $v_{s,n}$ is the normal critical velocity, v_1 and v_2 are the Poisson's ratio of tundish wall and inclusion, E_1 and E_2 are Young's modulus of tundish wall and inclusion, r_1 and r_2 is the Surface free energy of tundish wall and inclusion.

The restitution coefficient has been given in other works by Thornton *et al.*^[27,28] Meanwhile, Konstantopoulos^[29] believes that when the incident angle exceeds a critical angle, regardless of the incident velocity, it will not be captured by the wall, this article also takes this element into account and adds it to the mathematical model of wall boundary.

The inclusions entering the pouring chamber will rush toward the top slag under the drive of the molten steel, and be captured by the slag layer. The critical slip velocity given by Rückert^[30] is used to determine whether the inclusions have been captured:

$$\bar{u}_s = \frac{1}{18} d_p^2 \mathbf{g} \frac{\rho_l - \rho_p}{\mu_l}. \quad [16]$$

C. Calculation Process and Boundary Conditions

The calculation of the electromagnetic field is based on the finite element method, with the solution domain adopting tetrahedral unstructured adaptive meshing. As the channel serves as the primary site for induction heating, local refinement is carried out based on the calculated skin depth. The current density within the coil

is assumed to be uniformly distributed, and eddy currents at the coil and core are neglected, being converted into 10 pct power loss. Power levels of 600, 800, and 1000 kW are selected for the study, with a coil turn number of 46 and a frequency of 50 Hz. Magnetic parallel boundary conditions are applied at the surface of the air layer.

The calculations of fluid flow and heat transfer are based on the finite volume method. The fluid domain adopts a structured mesh. Due to the intense phenomena of flow, heat transfer, and inclusion collisions within the channel, the mesh in this area is refined. Due to the intense phenomena of flow, heat transfer, and inclusion collisions within the channel. The total number of mesh elements is 1,985,026. Initially, steady-state calculations for induction heating are conducted, and the results are utilized as the initial field for transient calculations. Subsequently, the computed electromagnetic force and joule heat are incorporated into the momentum and energy equations as source terms *via* User-Defined Functions (UDF). Building upon this, temperature and flow fields are solved based on LES. The solution process and details of the electromagnetic-thermo-hydrodynamic problem are depicted in Figure 4.

Finally, the motion, collision, and removal of inclusions are calculated using the DPM to derive removal rates for inclusions of different diameters and positions. Due to larger-size inclusions being predominantly removed during ladle refining processes, and the more pronounced motion and removal effect of smaller-size inclusions within the tundish wall and channel, seven diameters for investigation are selected: 3, 5, 10, 20, 30, 50 and 100 μm in this study. The injection method of inclusions is through surface injection, with a quantity of 10,000. The number of injections per time step is determined by the number of mesh on the inlet surface,

and the injection time stops when it reaches 10,000. The particle calculation time is 1000 seconds. The calculation process for adsorption and reflection of inclusions in contact with the wall of the tundish is shown in Figure 5. Computational parameters and boundary conditions are shown in Table III.

III. MODEL VALIDATION

Vives^[31] established a physical model of a channel induction furnace in 1990, as shown in Figure 6(a), and conducted a detailed study on the electromagnetic field of the induction furnace. The physical model of Vives and experimental results are used to verify the mathematical model established in this paper, with the validation of the flow field referenced to previous work on tundish in our laboratory.^[9] The comparison between Vives' experimental results and the numerical simulation results of this study is as follows: from Figure 6(b), it can be observed that in terms of the electromagnetic field, the electromagnetic field in the middle channel exhibits a spiral pattern with the center of the channel as the origin, showing a relatively regular distribution, with the outer intensity greater than the inner; however, in the left-side channel, due to skin effect and proximity effect, the magnetic field strength is greater on the side closer to the coil, exhibiting an eccentric distribution. The comparison results of electromagnetic forces, as shown in Figure 6(c), indicate that all electromagnetic forces are directed toward the interior of the channels. The electromagnetic force distribution in the middle channel appears relatively symmetric, while the left-side channel exhibits an eccentric distribution. Under identical physical models and boundary conditions, the distribution and numer-

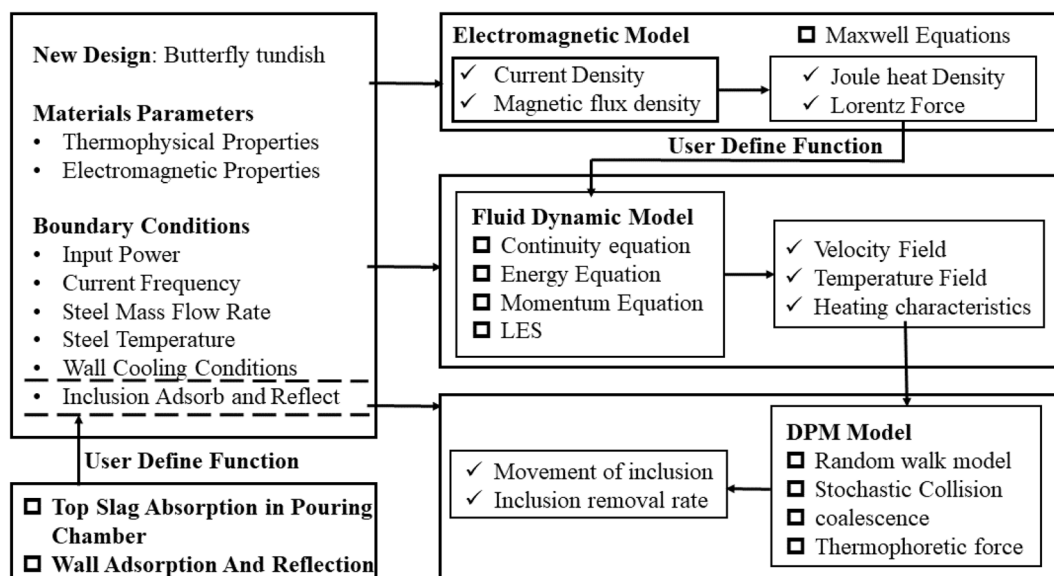


Fig. 4—Multi-physical fields calculation process.

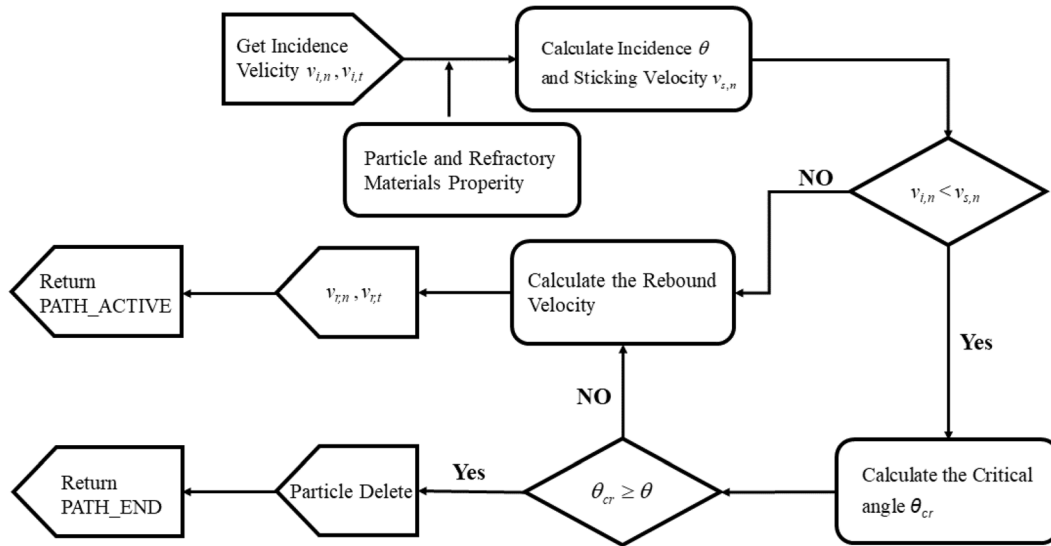


Fig. 5—Calculation process for inclusion removal.

Table III. Computational Parameters and Boundary Conditions

Parameter	Value
Molten Steel Mass Flow Rate/(kg s ⁻¹)	33.3
Induction Coil Current Frequency/(Hz)	50
Molten Steel Inlet Temperature/(K)	1833
Molten Steel Electric Conductive/(S m ⁻¹)	7.14 × 10 ⁵
Molten Steel Magnetic Conductive/(H m ⁻¹)	1.257 × 10 ⁻⁵
Molten Steel Density/(kg m ⁻³)	8523-0.8358T
Molten Steel Viscosity/(Pa s)	0.0061
Molten Steel Specific Heat/(J kg ⁻¹ K ⁻¹)	4320
Molten Steel Thermal Conductivity/(W m ⁻¹ K ⁻¹)	1300
Top Wall Heat Dissipation/(W m ⁻²)	15,000
Sidewall Heat Dissipation/(W m ⁻²)	4800
Bottom Wall Heat Dissipation/(W m ⁻²)	1800
Channel Wall Heat Dissipation/(W m ⁻²)	2000
Inclusion Density/(kg m ⁻³)	3900
Inclusion Diameter/(μm)	3/5/10/20/30/50/100

ical values of magnetic field intensity and electromagnetic forces obtained from experiments and numerical simulations are close. This confirms the accuracy of the electromagnetic field model and boundary conditions established in this paper.

IV. RESULTS AND DISCUSSION

A. Analysis of Electromagnetic Field

Figure 7 illustrates the induced current distribution within the butterfly-type tundish. Induced currents form a closed circuit across the pouring chamber, intermediate chamber, and two channels under the influence of an external magnetic field. The induced current concentrates within the channels, with only minor distribution elsewhere. Within the channels, the induced current exhibits an uneven distribution. This disparity is due to

the skin effect and proximity effect, where currents closer to the coil are stronger than those farther away, peaking at the channel's inlet and outlet. At induction heating powers of 600, 800, and 1000 kW, the induced current intensities along the axis measure 2.3×10^6 , 3.4×10^6 , and 4.6×10^6 A/m², respectively.

Figure 8 illustrates the distribution of the electromagnetic field, electromagnetic force, and joule heat in a butterfly-type tundish during induction heating. The figure indicates that similar to the distribution of induced current, the distribution of these three factors is affected by the skin effect and proximity effect. The values are highest within the skin layer near the coil and decrease as the distance from the coil increases. As depicted in Figure 8(a), it represents the vector of magnetic field intensity, following the experimental findings of Vives *et al.*,^[32–34] magnetic field lines are not only present within the coil but also permeate the

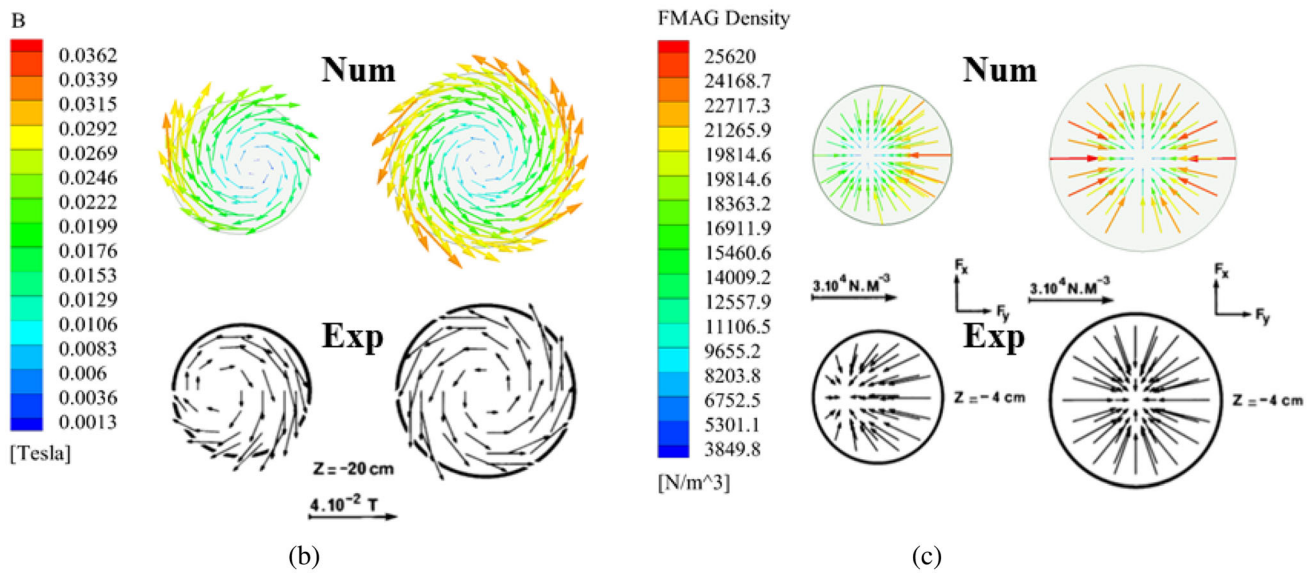
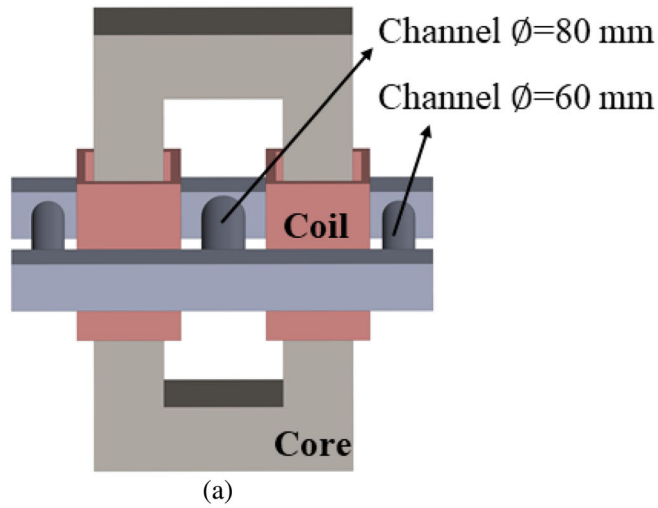


Fig. 6—Mathematical model validation: (a) The physical model used for verification, (b) Magnetic field strength verification, (c) Electromagnetic force verification.

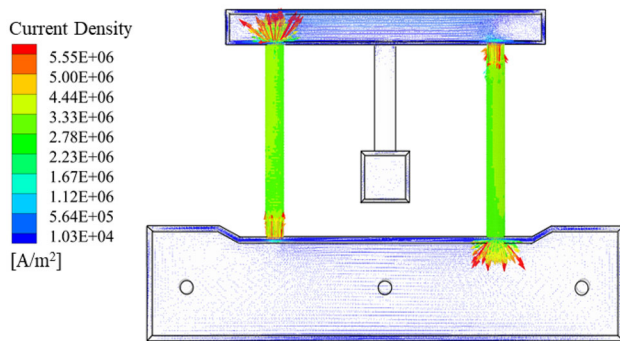


Fig. 7—Current density and vector diagram inside butterfly-type tundish.

entire tundish, reaching values up to the 10^{-2} magnitude level. Hence, if deemed necessary, shielding measures should be implemented for the measuring instruments.

Figure 8(b) depicts the distribution of electromagnetic force, directed toward the center of the channel, thereby exerting a clamping effect on the molten steel. Due to the eccentric force, the molten steel generates a swirling flow. Figure 8(c) illustrates the distribution of joule heat. As joule heat results from induced current and molten steel resistance, its distribution mirrors that of induced current, primarily concentrated within the channel. The areas where the steel is heated are also predominantly concentrated in the channel.

B. Analysis of Temperature and Flow Field

Figure 9 displays the temperature field of a butterfly-type tundish calculated at 1000 seconds using various induction heating powers. The molten steel enters from the inlet and flows out to the mold at the outlet, inevitably causing a temperature drop in other parts of the butterfly-type tundish as it passes through.

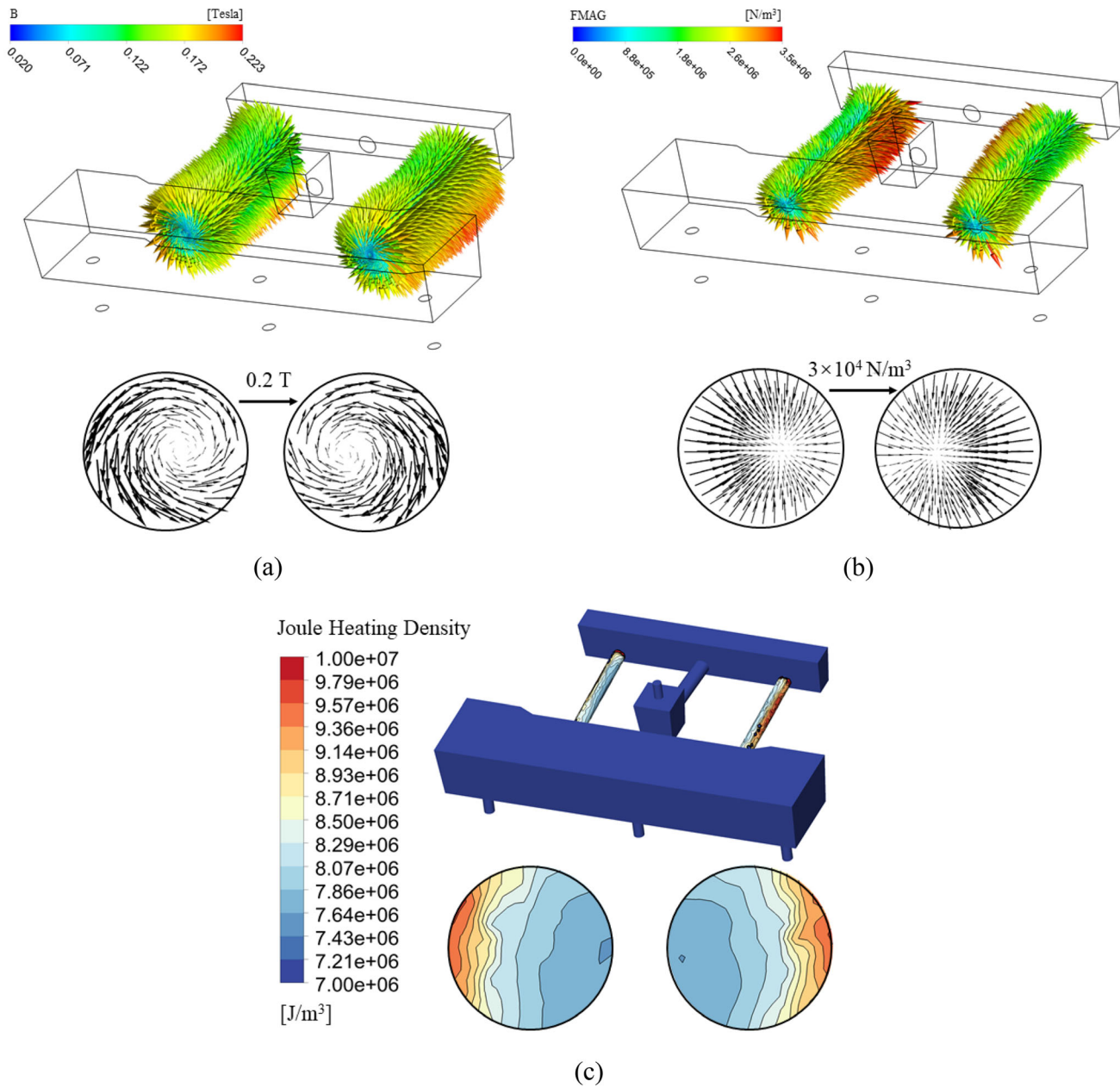


Fig. 8—Electromagnetic field calculation results: (a) Magnetic field intensity (b) joule Heating (c) Electromagnetic force.

Figure 9(a) shows the temperature distribution without using induction heating. It can be observed that the temperature continues to decrease as the flow progresses, resulting in the formation of wide-ranging low-temperature zones in the pouring chamber. When using induction heating, as shown in Figures 9(b) through (d), the temperature inside the channel rises significantly, and the temperature of the molten steel in the pouring chamber increases. At 600 kW, the temperature of most of the molten steel in the pouring chamber is close to or slightly higher than the inlet temperature, and the temperature compensation effect is significant. The higher the induction heating power, the more significant the temperature rise effect. Therefore, the induction heating power can be selected in reverse

according to the required to superheat inside the mold to control the temperature of the steel flowing into the mold to meet the requirements.

Figure 10 shows the temperature field on the cross section. As shown in Figure 10(a), Without induction heating, the temperature of the molten steel gradually decreases during the flow process. A low-temperature zone is formed in the upper and lower parts of the pouring chamber, with a maximum temperature difference of about 10 K and a temperature drop of approximately 7 K in the channel. As shown in Figures 10(b) through (d), the temperature field changes over time after using 800 kW induction heating. It can be seen that the channel is the main place for heating the molten steel, and the temperature of the molten steel is

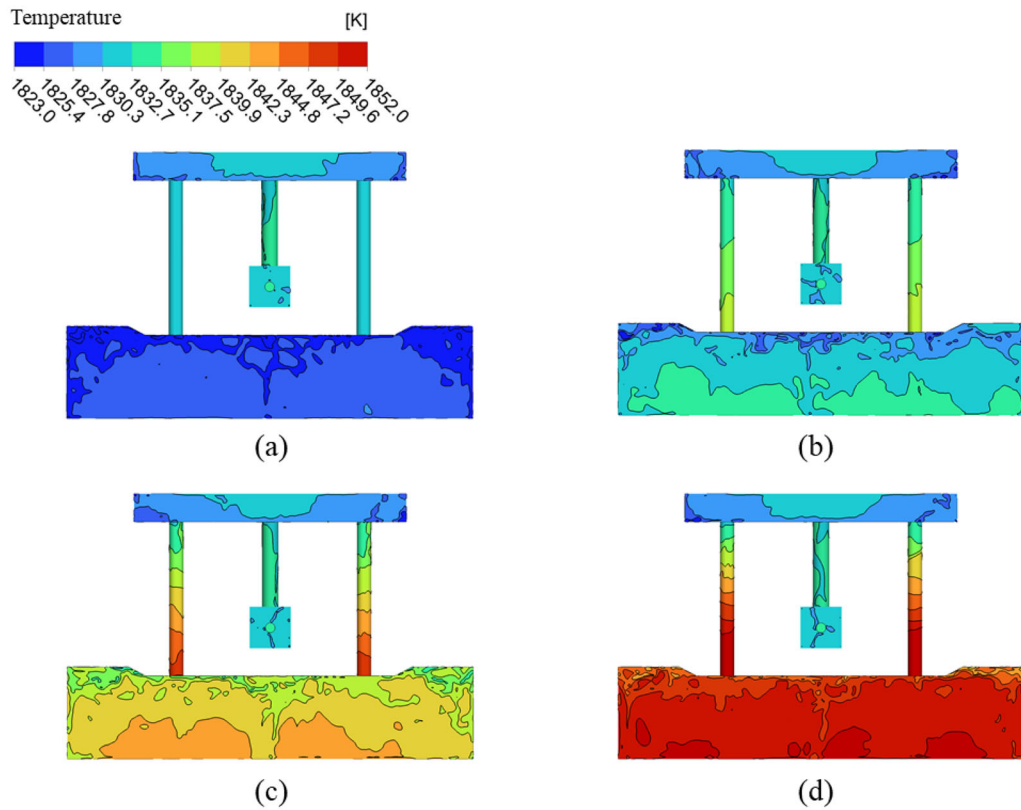


Fig. 9—The temperature field at 1000 s: (a) Without induction heating (b) 600 kW (c) 800 kW (d) 1000 kW.

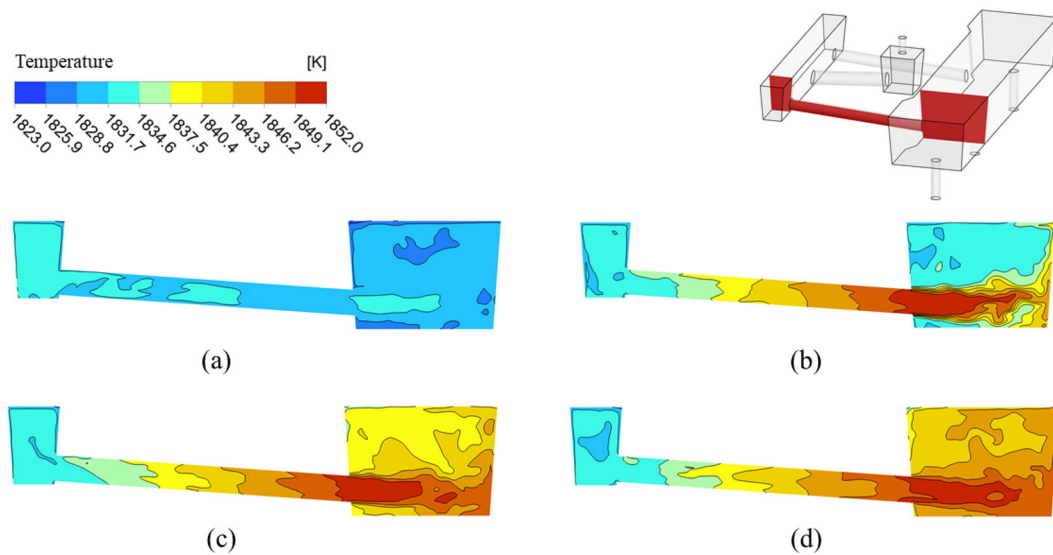


Fig. 10—Temperature field on cross section at different times: (a) 0 s (without induction heating) (b) 200 s (c) 600 s (d) 1000 s.

rapidly heated within the channel, with a temperature rise of about 24 K, the temperature of the steel flowing into the pouring chamber is much higher than that of the molten steel present in the pouring chamber. Therefore, the thermal buoyancy resulting from the density difference causes the molten steel to exhibit an upward flow effect, preventing direct impact on the wall

surface and reducing erosion of the refractory material. This effect also prolongs the molten steel's movement path, promotes temperature homogenization, and increases the residence time of the molten steel in the tundish, thereby facilitating the upward floating removal of inclusions. When the calculation time reaches 1000 seconds, the low-temperature zone dissipates, and the

lowest temperature in the pouring chamber stabilizes at about 1840 K, indicating that the heat loss of the molten steel has been fully compensated.

Figure 11 depicts the outlet heating process curve of the butterfly-type tundish during the calculation of 1000 seconds under various induction heating powers. The heating curve serves as a crucial parameter for the tundish, determining whether the steel entering the mold meets the superheat requirements, thereby influencing the solidification process within the mold.^[35] As can be seen from Figure 11(a), when there is no induction heating, the temperature drop of the molten steel caused by the heat dissipation of the sidewalls and top slag cannot be replenished in time, so the temperature of the molten steel will continue to decrease and reach basic equilibrium after 1000 seconds, with a temperature drop amplitude of 15 K. When using induction heating, the outlet temperature gradually increases and reaches equilibrium after 1000 seconds. When the induction heating power is 600, 800, and 1000 kW, the average temperature rise of the three outlets is 7 K, 15 K, and 26

K, respectively. Due to the stochastic nature of turbulence and the vigorous mixing of molten steel in the pouring chamber, the temperatures of the three outlets vary. As outlet 2 is positioned between outlet 1 and outlet 3, its temperature is slightly higher than that of the other two. A temperature difference exceeding 3 K between outlets is considered detrimental.^[36] It is notable that the maximum temperature difference among the outlets of the butterfly-type tundish consistently stays within 3 K, affirming the soundness of the physical model design.

Figure 12 illustrates the flow field within the tundish both without induction heating and with 800 kW induction heating. In the channel, induction heating causes the molten steel to develop a swirling flow due to the electromagnetic forces deflecting from the center. The maximum tangential velocity reaches approximately 0.25 m/s under induction heating, whereas without induction heating, the tangential velocity is nearly negligible. The presence of tangential velocity can extend the residence time of molten steel in the channel,

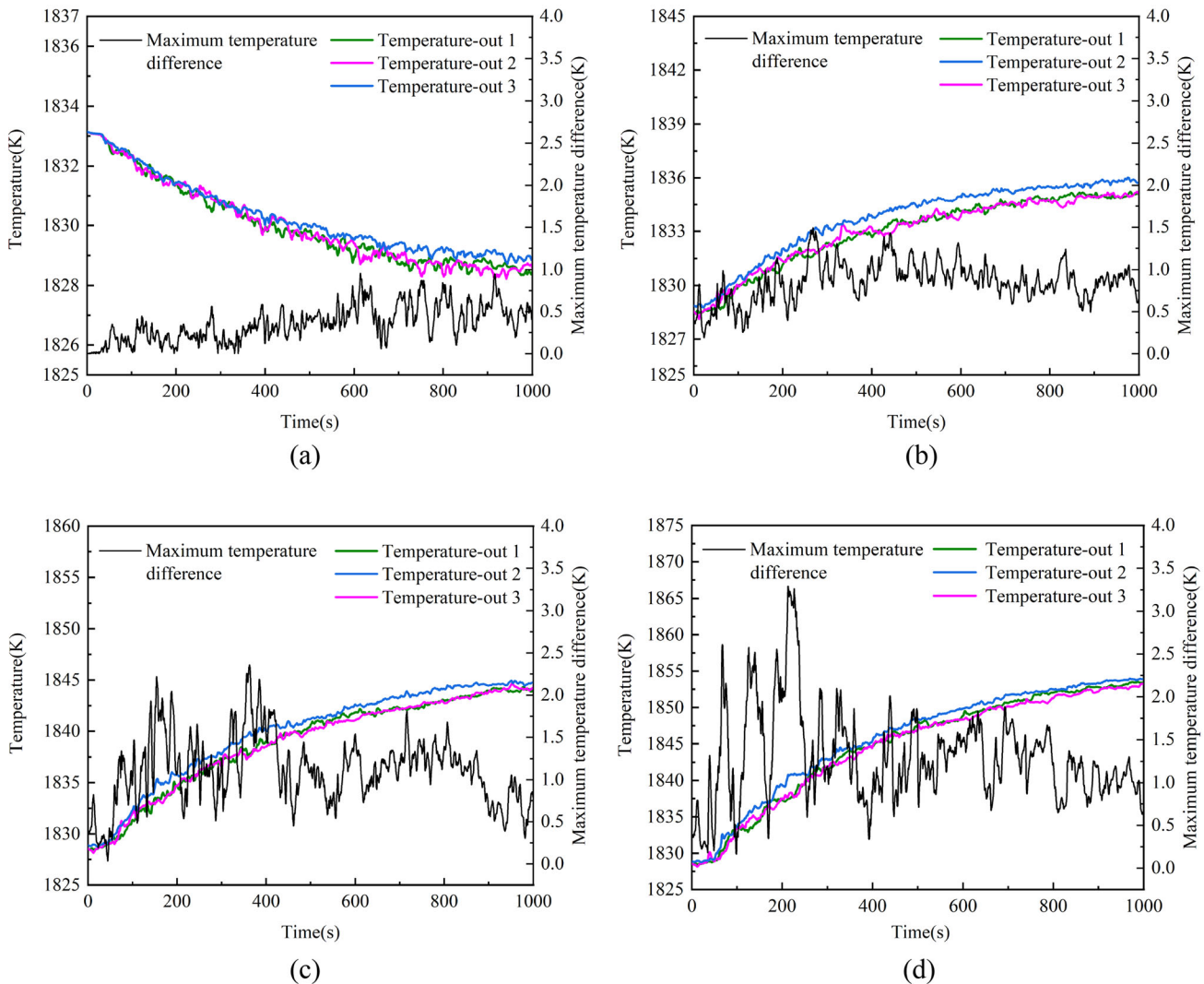


Fig. 11—Outlet temperature and maximum temperature difference at outlet: (a) Without induction heating (b) 600 kW (c) 800 kW (d) 1000 kW.

facilitating the movement of inclusions toward the wall. This increases the likelihood of inclusions being captured by the wall, thereby enhancing the removal rate of inclusions within the channel. In the pouring chamber, the acceleration effect of electromagnetic force on the molten steel in the channel maintains swirling inertia even after the molten steel flows out of the channel. This creates a stirring effect on the molten steel in the pouring chamber, resulting in a more active flow field within the pouring chamber.

Figure 13 depicts the flow field inside the tundish under conditions of no induction heating and 800 kW induction heating. Streamlined results on the cross section reveal the presence of large and small vortices in multiple parts of the pouring chamber without induction heating, leading to insufficient flow activity and easy formation of dead zones. However, upon using 800 kW induction heating, the area where vortices form is significantly reduced, replaced by a broader circulation range. Vorticity, which represents the process of vortex generation, evolution, and dissipation in a fluid, is indicative of flow activity. A higher vorticity indicates more active flow, with increased vortex generation frequency promoting the mixing of cold and hot fluids, enhancing temperature homogenization, and stabilizing the temperature of the steel entering the mold.^[37] Indeed, the vorticity and its distribution range under 800 kW induction heating are substantially larger compared to those without induction heating. Consequently, the temperature field of the steel in the pouring chamber during induction heating is notably improved.

C. Movement and Removal of Inclusions

Figure 14 depicts the movement of molten steel and inclusions in the channel under no induction heating and 800 kW induction heating. In Figure 14(a), it is evident that without induction heating, noticeable boundary layers exist in both the upper and lower parts of the channel. The flow velocity of molten steel in these

boundary layers is relatively low, and the velocity vector near the boundary layer is parallel to the wall. This orientation makes it challenging for inclusions to penetrate the boundary layer and make contact with the wall. Similarly, Li^[38] argued that the radial velocity of particle movement, as it approaches the wall, is predicted to decrease due to wall effects, which is one of the important reasons for the low removal rate in the channel without induction heating. Figure 14(b) illustrates that under the influence of the eccentric electromagnetic force generated by induction heating technology, the steel flow becomes intricate, exhibiting a spiral forward motion as depicted in Figure 12. This dynamic flow pattern facilitates the breakthrough of inclusions through the boundary layer, leading to collisions with the wall. Subsequently, these collisions result in kinetic energy loss upon rebound, ultimately enabling the wall to capture the inclusions and thereby enhancing the removal rate. In Figure 14(a), it is evident that without induction heating, inclusions primarily accumulate near the axis of the channel. They subsequently flow slowly through the channel alongside the molten steel into the pouring chamber. However, with induction heating, as depicted in Figure 14(b), the tangential motion range of inclusions expands, significantly increasing their frequency of collision with the wall. Upon colliding with the wall, the velocity of inclusions decreases, while those near the axis, unable to contact the wall, experience acceleration.

Figure 15 presents several typical methods for removing inclusions in a butterfly-type tundish and illustrates the positions where inclusions are adsorbed. Figures (a) through (d) depict four inclusion removal methods, along with the trajectory from inlet to disappearance. From Figure 15(a), it can be inferred that wall adsorption occurs at various locations within the butterfly-type tundish. In the injection chamber, inclusions are primarily adsorbed at the junction of six surfaces. In the middle chamber, inclusions tend to be adsorbed near the bottom of the channel, while in the pouring chamber,

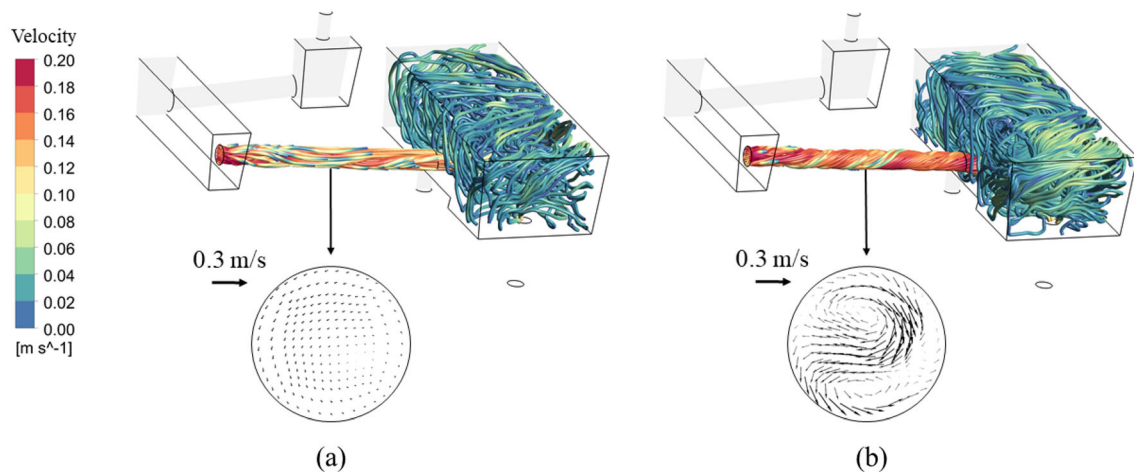


Fig. 12—Flow field and velocity vector inside the channel: (a) Without induction heating (b) Induction heating power of 800 kW.

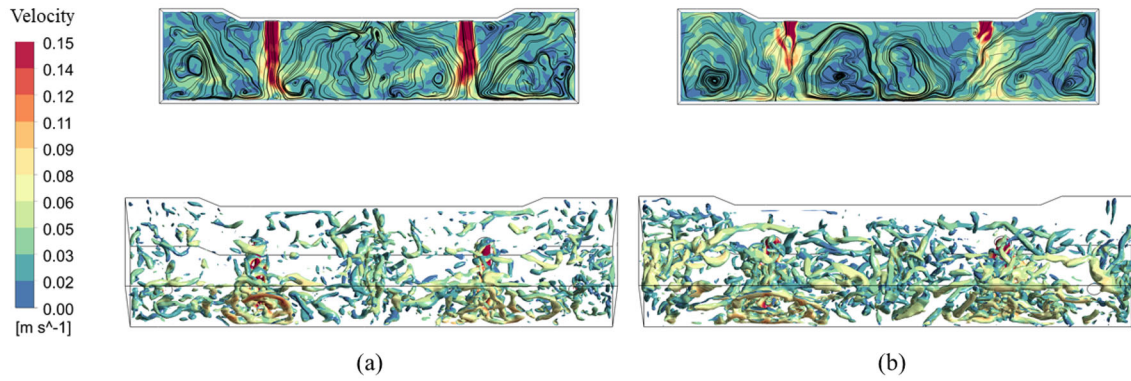


Fig. 13—Streamline and vortex distribution in pouring chamber: (a) Without induction heating (b) Induction heating power of 800 kW.

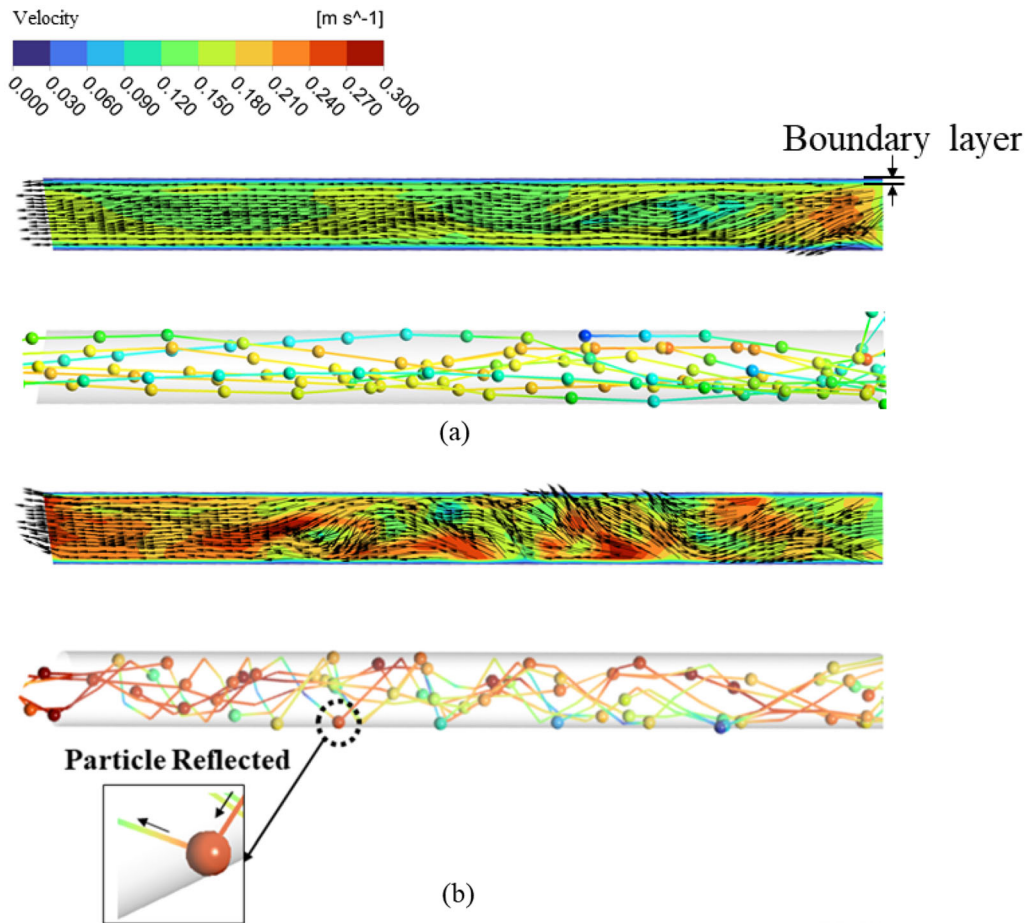


Fig. 14—The movement of molten steel and inclusions in the channel: (a) Without induction heating (b) Induction heating power of 800 kW.

they are mainly adsorbed on the bottom surface. Lower molten steel flow rates result in lower inclusion velocities, making them more prone to adsorption. Consequently, these positions typically coincide with flow dead zones. In Figure 15(b), it is evident that the majority of inclusions adsorbed in the channel are concentrated in the first half, with a decrease in adsorption observed in the second half. The reason for this phenomenon is that the low flow rate near the

channel in the middle chamber results in slower movement of inclusions entering the channel. This will result in a large number of inclusions being directly adsorbed. And then, due to the existence of channel inclination angle, the steel liquid will continuously accelerate, which will drive the movement of unadsorbed inclusions and make it difficult to reach the velocity threshold. Finally, in Figure 15(c), the distribution of inclusions adsorbed by the top slag layer appears relatively uniform, with

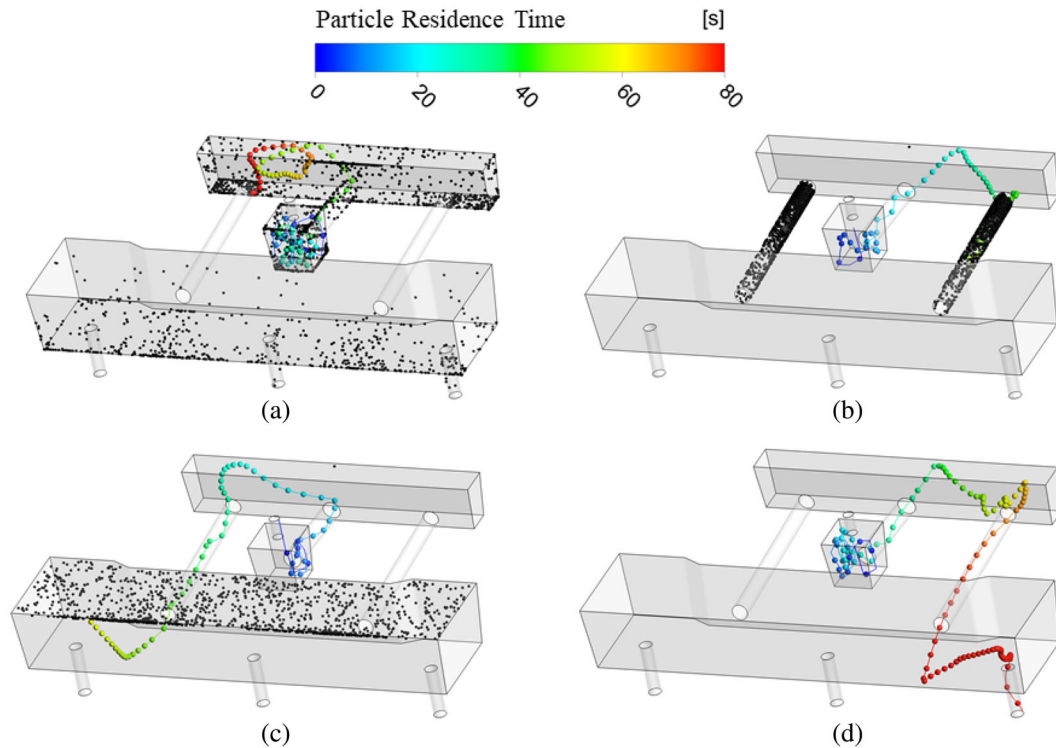


Fig. 15—The removal method and location of inclusions in butterfly-type tundish: (a) Adsorbed on tundish wall (b) Adsorbed on the channel (c) Adsorbed in slag layer (d) Escaped through the outlet.

more inclusions observed at locations where the upwelling stream impacts the slag layer compared to surrounding areas.

Figure 16 illustrates the total removal rate of inclusions and the removal rates in different parts of the butterfly-type tundish, as well as the total removal rate at different induction heating powers. The implementation of induction heating technology markedly enhances the removal rate of inclusions, with higher power levels demonstrating a more pronounced removal effect. At induction heating powers of 0, 600, 800, and 1000 kW, the total inclusion removal rates in the butterfly-type tundish are 69.18, 83.37, 87.69, and 92.01 pct, respectively. Without induction heating, inclusion removal primarily occurs through adhesion to the wall surface. Additionally, the narrow confines of the channel contribute significantly to inclusion removal. However, because the molten steel in the channel lacks sufficient temperature rise, the upward flow momentum as it enters the pouring chamber from the outflow channel is limited. This limitation makes it challenging for the molten steel to reach the top slag and become captured by the slag layer. Hence, the removal rate in the top slag is relatively low. Increasing the induction heating power to 600 kW significantly boosts the contribution of the top slag to the inclusion removal rate by approximately 8.5 pct, attributed to the presence of upward flow in the pouring chamber. Simultaneously, there is a notable enhancement in the removal rate of inclusions in the channel, approximately 13.2 pct. Further escalation of the induction heating power results in a higher percentage of inclusions being adsorbed in both the top slag and

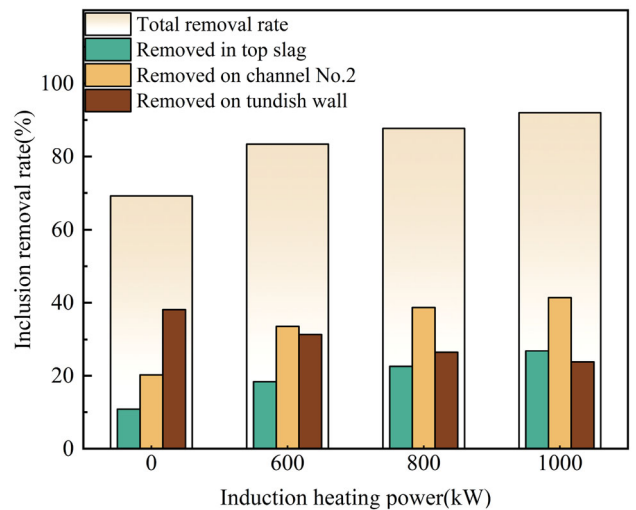


Fig. 16—The removal rates of inclusions in different locations.

channel. Specifically, compared to 600 kW, the removal rate in the top slag increases by 4.2 and 8.5 pct at 800 and 1000 kW, respectively. However, the increase in channel adsorption slows down, compared to 600 kW, the increase at 800 kW is 5.1 pct, while compared to 800 kW, the increase at 1000 kW is only about 2.7 pct. The adsorption effect of inclusions on the wall diminishes with the rise in induction heating power, primarily observed on the wall of the pouring chamber. This decline occurs because, with induction heating, most inclusions are captured by the wall before entering the

pouring chamber and in the top slag region of the pouring chamber, reducing the amount captured by the wall.

Figure 17 illustrates the relationship between the removal rates of inclusions and their diameters at various positions in the butterfly-type tundish under different induction heating powers. As depicted in Figure 17(a), the quantity of inclusions adhered to the wall of the butterfly-type tundish exhibits a negative correlation with diameter. This observation aligns with the findings of Thornton and Raymond^[39] who proposed that the critical adhesion velocity is inversely related to the radius. The higher the induction heating power, the fewer inclusions are adsorbed on the wall since most of the inclusions are absorbed in the channel and top slag layer. Figure 17(b) illustrates that larger diameter inclusions are more readily removed in the channel, a trend that becomes more pronounced with increased induction heating power. Besides velocity, maximizing collisions with the wall is crucial for inclusion removal in the channel. Larger inclusions experience heightened thermophoretic force and electromagnetic force, coupled with greater inertia, thus increasing the likelihood of contact, rebound, and subsequent adsorption onto the wall. As depicted in Figure 17(c), the ratio of inclusions adsorbed in the top slag layer positively correlates with both the induction heating power and inclusion diameter. With higher induction heating power, the temperature of the molten steel entering the pouring chamber through the outflow channel increases. The increased thermal buoyancy of the molten steel, resulting from the density difference induced by temperature variance, enhances the upward velocity of inclusions. Consequently, they surpass the critical velocity threshold and enter the slag layer. Indeed, the larger the diameter of the inclusions, the more pronounced the buoyancy effect they experience, facilitating their movement toward the slag layer. Consequently, the likelihood of larger inclusions being adsorbed by the slag layer is significantly heightened due to the combined influence of multiple factors. However, there is a deviation in this trend observed at a diameter of 100 μm . This anomaly arises because a substantial portion of 100 μm inclusions is removed within the channel, with only a minor fraction entering the pouring chamber.

Figure 18 illustrates the percentage of inclusions of various diameters escaping from the outlet of the butterfly-type tundish and entering the mold relative to the total number of inclusions, under different induction heating powers. With increasing induction heating power, there is a notable decrease in the number of inclusions of varying diameters entering the mold, particularly when compared to non-induction heating conditions. The implementation of induction heating technology significantly reduces this proportion. Moreover, without induction heating, the diameter distribution of inclusions entering the mold is relatively uniform, with larger inclusions being inadequately removed, which increases the burden of inclusion removal in the mold and seriously affects the quality of the casting billet.^[40,41] After using induction heating

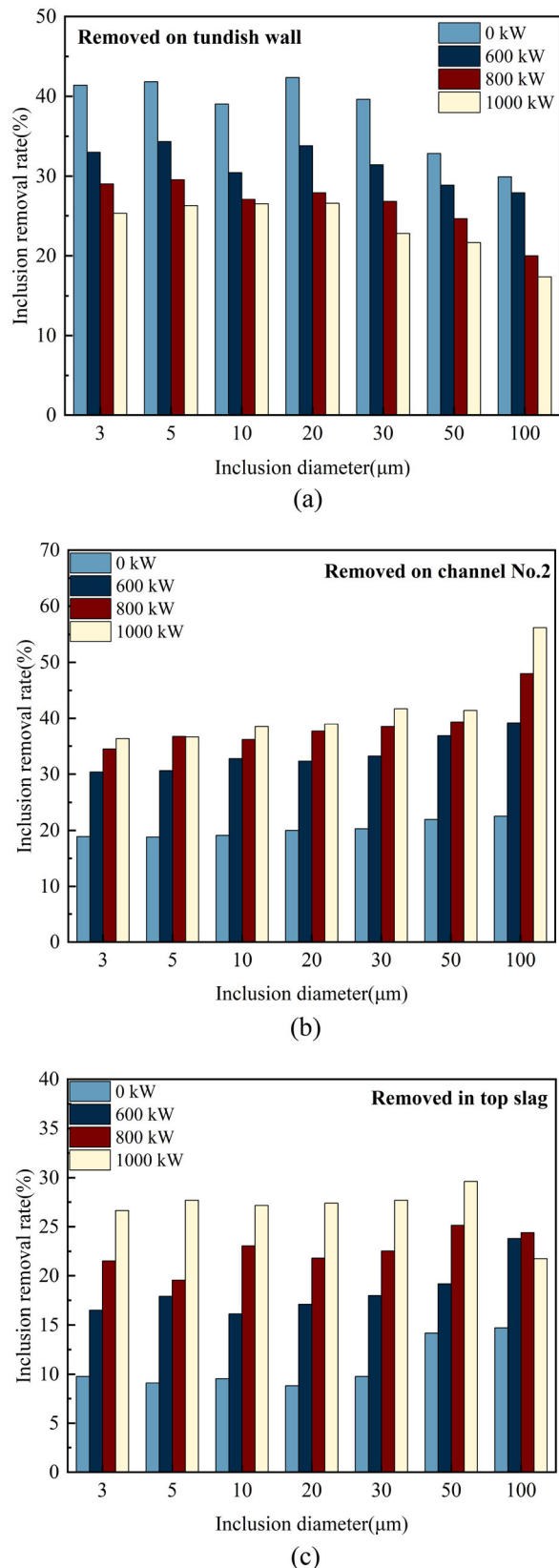


Fig. 17—The removal rate of inclusions in different locations of butterfly-type tundish: (a) Removed on tundish wall (b) Removed on the channel (c) Removed in top slag layer.

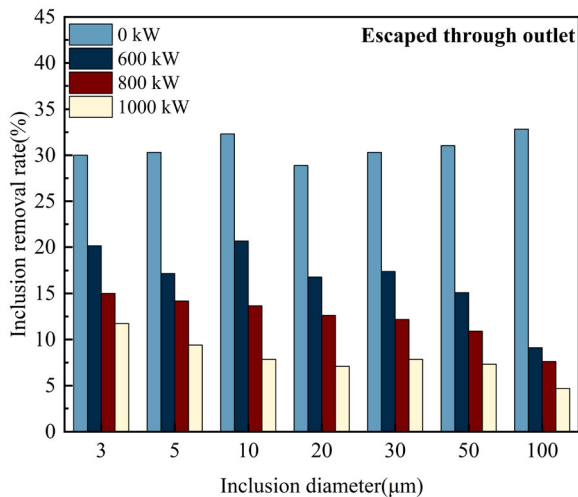


Fig. 18—The relationship between the diameter distribution of inclusions escaped through the outlet and the induction heating power.

with 600, 800, and 1000 kW, taking 100 μm as an example, this number decreased by about 24, 26, and 30 pct respectively, and the effect was very significant.

V. CONCLUSIONS

This study tackles the retrofitting issues of conventional non-induction heating tundish through the design of a butterfly-type induction heating tundish model. A three-dimensional coupled mathematical model encompassing thermo-electromagnetic-hydrodynamic-inclusion movements was developed to analyze the electromagnetic field, flow field, temperature distribution, heating characteristics, and inclusion removal rate. The following conclusions were drawn:

- (1) The induced current forms a closed loop within the butterfly-type tundish. The distribution of induced current, electromagnetic force, and joule heating is similar, with the effects of skin effect and proximity effect causing them to be greater on the side closer to the coil than on the side farther away. They are primarily concentrated within the channel. The electromagnetic force within the channel exhibits an eccentric state.
- (2) The process of induction heating primarily occurs within the channel, where the molten steel undergoes a spiral motion under the influence of electromagnetic forces. Upon entering the pouring chamber, the upward flow formed optimizes the flow field, promotes the mixing of hot and cold molten steel, and extends residence time. The temperature rise at the outlet is -15 K , 7 K , 15 K , and 26 K at 0, 600, 800, and 1000 kW, respectively, effectively compensating for temperature losses.
- (3) Induction heating significantly improves the removal rate of inclusions. At heating powers of 0, 600, 800, and 1000 kW, the total removal rates of inclusions are 69.18, 83.37, 87.69, and 92.01 pct,

respectively. The channel serves as the primary site for inclusion removal.

- (4) The removal rates within the channel and the slag layer are positively correlated with the inclusion diameter, while the removal rate at the wall is negatively correlated. The distribution of escaped inclusion diameter at the outlet is relatively uniform without induction heating, whereas with induction heating, the proportion of large-size inclusions sharply decreases.

ACKNOWLEDGMENTS

This work was supported by the Liaoning Xingliao Talents-Top-notch Young Talents Project (No. XLYC 2203064) and the Excellent Youth Fund of Liaoning Natural Science Foundation (No. 2023JH3/10200001). The authors are grateful for their financial support.

CONFLICT OF INTEREST

On behalf of all authors, the corresponding author states that there is no conflict of interest.

REFERENCES

1. J. Wang, W. Liu, S. Yang, X. Zuo, L. Zhao, and J. Li: *Metall. Mater. Trans. B*, 2024, vol. 55B, pp. 808–20.
2. B. Zhao, B.G. Thomas, S.P. Vanka, and R.J. O'Malley: *Metall. Mater. Trans. B*, 2005, vol. 36B, pp. 801–23.
3. X. Huang, B.G. Thomas, and F.M. Najjar: *Metall. Trans. B*, 1992, vol. 23, pp. 339–56.
4. H. Zhang, Q. Fang, C. Liu, J. Wang, and C. Liu: *Metall. Res. Technol.*, 2022, vol. 119, p. 317.
5. A. Braun, M. Warzecha, and H. Pfeifer: *Metall. Mater. Trans. B*, 2010, vol. 41B, pp. 549–59.
6. C. Chen, L.T.I. Jonsson, A. Tilliander, G. Cheng, and P.G. Jönsson: *Metall. Mater. Trans. B*, 2015, vol. 46B, pp. 169–90.
7. M.A. Barron-Meza, J.D.J. Barreto-Sandoval, and R.D. Morales: *Metall. Mater. Trans. B*, 2000, vol. 31B, pp. 63–74.
8. S.V. Ramos, P. Cisquini, B.M. Braga, J.R. Oliveira, A.L. Silva, and M.C. Bagatini: *Metall. Mater. Trans. B*, 2023, vol. 54B, pp. 230–48.
9. Q. Wang, B. Li, and F. Tsukihashi: *ISIJ Int.*, 2014, vol. 54, pp. 311–20.
10. Q. Yue, C.B. Zhang, and X.H. Pei: *Ironmak. Steelmak.*, 2017, vol. 44, pp. 227–36.
11. X. Chen, H. Xiao, P. Wang, H. He, H. Tang, and J. Zhang: *Steel Res. Int.*, 2022, vol. 93, p. 2100839.
12. H. Zhang, H. Lei, C. Ding, S. Chen, H. Niu, and B. Yang: *Steel Res. Int.*, 2022, vol. 93, p. 2200181.
13. A. Tripathi: *Appl. Math. Model.*, 2011, vol. 35, pp. 5075–90.
14. Q. Wang, F. Qi, B. Li, and F. Tsukihashi: *ISIJ Int.*, 2014, vol. 54, pp. 2796–2805.
15. L. Zhang, S. Taniguchi, and K. Cai: *Metall. Mater. Trans. B*, 2000, vol. 31B, pp. 253–66.
16. H. Lei, B. Yang, Q. Bi, Y. Xiao, S. Chen, and C. Ding: *ISIJ Int.*, 2019, vol. 59, pp. 1811–19.
17. F. Xing, S. Zheng, and M. Zhu: *Steel Res. Int.*, 2018, vol. 89, p. 1700542.
18. X. Chen, P. Wang, H. Xiao, B. Yi, H. Tang, and J. Zhang: *J. Mater. Res. Technol.*, 2023, vol. 24, pp. 1410–28.
19. M. Warzecha, T. Merder, P. Warzecha, and G. Stradomski: *ISIJ Int.*, 2013, vol. 53, pp. 1983–92.
20. F. Wang, B. Li, and F. Tsukihashi: *ISIJ Int.*, 2007, vol. 47, pp. 568–73.

21. P.K. Jha, R. Ranjan, S.S. Mondal, and S.K. Dash: *Int. J. Numer. Methods Heat Fluid Flow.*, 2003, vol. 13, pp. 964–96.
22. N. Alkishriwi, M. Meinke, W. Schröder, A. Braun, and H. Pfeifer: *Steel Res. Int.*, 2006, vol. 77, pp. 565–75.
23. K. Takahashi and S. Taniguchi: *ISIJ Int.*, 2003, vol. 43, pp. 820–27.
24. L. Li, B. Li, and Z. Liu: *ISIJ Int.*, 2017, vol. 57, pp. 1980–89.
25. L. Li, Z. Liu, M. Cao, and B. Li: *JOM*, 2015, vol. 67, pp. 1459–67.
26. C. Thornton and Z. Ning: *Powder Technol.*, 1998, vol. 99, pp. 154–62.
27. C. Wu, L. Li, and C. Thornton: *Int. J. Impact Eng.*, 2003, vol. 28, pp. 929–46.
28. C. Thornton, Z. Ning, W. Chuan-yu, M. Nasrullah, and L. Long-yuan: in *Granular Gases*, T. Pöschel and S. Luding, eds., vol. 564, Springer, Berlin, 2001, pp. 184–94.
29. A.G. Konstandopoulos: *J. Aerosol Sci.*, 2006, vol. 37, pp. 292–305.
30. A. Rückert: *Steel Res. Int.*, 2009, vol. 80, pp. 568–74.
31. C. Vives and R. Ricou: *Metall. Trans. B*, 1991, vol. 22, pp. 193–209.
32. C. Vives: *Metall. Trans. B*, 1989, vol. 20, pp. 623–29.
33. J.L. Meyer, J. Szekeley, N. El-Kaddah, C. Vivès, and R. Ricou: *Metall. Trans. B*, 1987, vol. 18, pp. 539–48.
34. C. Vivès: *Metall. Mater. Trans. B*, 1996, vol. 27B, pp. 457–64.
35. C. Wang, Z. Liu, B. Li, and J. Xu: *Metall. Mater. Trans. B*, 2023, vol. 54B, pp. 1275–89.
36. P. Wang, X. Chen, H. Xiao, X. Li, Z. Ma, H. Tang, and J. Zhang: *Ironmak. Steelmak.*, 2021, vol. 48, pp. 1200–10.
37. C. Wang, Z. Liu, and B. Li: *Metall. Mater. Trans. B*, 2023, vol. 54B, pp. 3438–50.
38. M. Li and R.I.L. Guthrie: *Metall. Mater. Trans. B*, 2000, vol. 31B, pp. 357–64.
39. R.M. Brach and P.F. Dunn: *Aerosol Sci. Technol.*, 1992, vol. 16, pp. 51–64.
40. Z. Liu, B. Li, L. Zhang, and G. Xu: *ISIJ Int.*, 2014, vol. 54, pp. 2324–33.
41. Z. Liu and B. Li: *Powder Technol.*, 2016, vol. 287, pp. 315–29.

Publisher's Note Springer Nature remains neutral with regard to jurisdictional claims in published maps and institutional affiliations.

Springer Nature or its licensor (e.g. a society or other partner) holds exclusive rights to this article under a publishing agreement with the author(s) or other rightsholder(s); author self-archiving of the accepted manuscript version of this article is solely governed by the terms of such publishing agreement and applicable law.